Supplement of Atmos. Chem. Phys., 22, 12629–12646, 2022
https://doi.org/10.5194/acp-22-12629-2022-supplement

Supplement of

Seasonal modeling analysis of nitrate formation pathways in Yangtze River Delta region, China

Jinjin Sun et al.

Correspondence to: Jianlin Hu (jianlinhu@nuist.edu.cn) and Momei Qin (momei.qin@nuist.edu.cn)

Supplementary Material

Section I: Introduction

1.1.Conceptual framework of the day-night chemical pathways of NO_3^-.

Nitrate might be produced through the following eight reactions pathways. The chemical equations for these eight production reactions pathways are written as follows:

$NO_2 + OH \rightarrow HNO_3$ *R1*

$NO_2 + O_3 \rightarrow NO_3 + O_2$ *R2*

$NO_2 + NO_3 \leftrightharpoons N_2O_5$ *R3*

$NO_2 \rightarrow 0.5HNO_3 + 0.5HONO$ *R4*

$N_2O_5 + H_2O(g) \rightarrow 2HNO_3$ *R5*

$N_2O_5 + H_2O/Surf \rightarrow 2HNO_3$ *R6*

$NO_3 + HO_2 \rightarrow 0.2HNO_3 + 0.8OH + 0.8NO_2$ *R7*

$NO_3 + VOC_S \rightarrow HNO_3$ *R8*

$NO_3 \rightarrow HNO_3$ *R9*

$TNO_3 \rightarrow HNO_3$ *R10*

$HNO_3(g) + NH_3(g) \rightarrow NH_4^+(p) + NO_3^-(p)$ *R9*

Section II: Methods

2.1. The Optimized WRF model configurations

The major physics schemes used were the New Thompson et al. scheme, the Noah Land Surface Model, the Mellor-Yamada-Janjic planetary boundary layer (PBL) scheme, and the rapid radiative transfer model (RRTM) longwave and shortwave radiation scheme. Detailed WRF model configurations were shown in Table S1 and follow the previous studies by (Hu et al., 2016; Liu et al., 2020; Wang et al., 2021). Common statistics for WRF-CMAQ model performance included mean bias (MB), normalized mean bias (NMB), normalized mean error (NME), correlation coefficient (R), root mean square error (RMSE) and index of agreement(IOA). The definitions and criteria of statistic metrics were shown in Table S4.

2.2 Observation data and Statistics for model performance

Hourly O_3, NO_2 and $PM_{2.5}$ observation data at five environmental monitoring sites

(Shanghai, Nanjing, Hangzhou, Heifei and Changzhou) in the YRD (Fig. 1) were obtained from the China Ministry of Ecology and Environment (MEE). As well as NO_3^-, hourly $PM_{2.5}$ chemical compositions were collected from the Pudong supersite in Shanghai (31°23'N, 121°54'E), Chaohui District 5 in Hangzhou (30°29'N, 120°16'E), Pearl Plaza in Heifei (31°78'N, 117°20'E) and Changzhou monitoring site (31°76'N, 119°96'E). The Pudong site (31°23'N, 121°54'E) is an urban site located near the Century Avenue with heavy traffic, and it is only ~3 km from the business center Lujiazui. The instruments at this site were located on the roof of a 20 m tall building.

2.3. The calculation of local, direct and indirect transport contributions to the rate of TNO_3 production reactions

Further descriptions of the contribution to TNO_3 production pathways are provided in the Section S2.3. In WRF-CMAQ modeling, the PA tool was used to calculate the rates of all TNO_3 production reactions. Modeled rates of a specific reaction in the Base, YRD-zero, Outside-zero and All-zero scenarios (definitions shown in the section 2.2) were marked as R_{base}, $R_{\mathrm{YRD-zero}}$, $r_{\mathrm{outside-zero}}$, and $R_{\mathrm{all-zero}}$, respectively, and all expressed as mean rates in Shanghai. The rates related to local, direct and indirect transport contributions (denoted as R_{Local}, R_{Direct} and R_{Indirect}) can be calculated using the same method as the calculation of pollutant contributions.

$$R_{\mathrm{Local}} = (R_{\mathrm{outside-zero}} - R_{\mathrm{all-zero}}) \quad (1)$$

$$R_{\mathrm{Direct}} = (R_{\mathrm{YRD-zero}} - R_{\mathrm{all-zero}}) \quad (2)$$

$$R_{\mathrm{Indirect}} = (R_{\mathrm{base}} - R_{\mathrm{outside-zero}}) - (R_{\mathrm{YRD-zero}} - R_{\mathrm{all-zero}}) \quad (3)$$

(1) R_{Local}: air pollutants directly emitted by sources within target regions and chemically produced from locally emitted precursors.

(2) R_{Direct} represents that key precursors emitting from outside regions, including the directly transported and formed through chemical reactions from outside precursors.

(3) R_{Indirect} represents that locally emitted NOx reacts with transported O_3.

The sum of R_{Direct} and R_{Indirect} is the contribution of regional transport.

Section III: Results and discussion

3.1 CMAQ model performance

Generally, in Fig. S2, the hourly time series of predicted and observed NO_3^- concentrations are well-captured in the winter of Shanghai (NMB = -0.20, MB = -2.09, and R = 0.55), the autumn of Hefei (NMB = -0.07, MB = -0.68, and R = 0.56), and the spring of Hangzhou (NMB = -0.20, MB = -1.71, and R = 0.44).

3.2 Regional transport contribution to nitrate

In Fig. S3, the higher predicted NO_3^- levels occur in the NCP (Heinan, Heibei and Shangdong provinces) than in the YRD. In winter, spring, summer and autumn, the contribution of background, local, direct and indirect transport to nitrate-related species (O_3, HNO_3, $PM_{2.5}$, NO_3^-, NO_2, NH_3, SO_4^{2-}, and SOC) in Shanghai are shown in Fig. S4. For NO_3^-, local emissions dominated regional NO_3^- concentration (45–76 %), while regional transport contributed 21–54% to nitrate in all seasons, with indirect transport dominating the regional transport of NO_3^-. Higher contributions of indirect nitrate transport occurred in January (31%) and April (34%), suggesting the important role of transported precursor for NO_3^- production during the periods. Fig. S4c shows that most of the precursors (NO_2: 96–99% and NH_3: 98–100%) are dominantly attributed to local contributions. For O_3, direct transport contributed 15-32% to regional concentration during the periods (Fig. S4b). Local emissions and indirect transport led to the depletion of O_3, which was indicated by the negative contributions in January, April, and October. The negative contributions to O_3 could be justified in two ways. Firstly, locally emitted NO_2 could react with transported O_3 to produce nitrate via the Het N_2O_5 pathway at night. Alternatively, the strong titration of transported O_3 by local NO at the surface layer could also lead to the consumption of O_3. Contrary to other periods, local emissions contributed 45% to O_3 production in July, which was later transported to external regions.

In addition, HNO_3 was dominated by the contributions of local emissions and direct transport. In January, April and October, higher contributions by direct transport to HNO_3 are observed in Fig. S5a. However, the spatial distributions of HNO_3 show that higher HNO_3 concentration are found in July, which was consistent with the stronger chemical production rates. Similar to NO_3^-, local emissions in the YRD region were responsible for higher HNO_3 concentrations. In the same vein, local emissions also dominated the contributions to $PM_{2.5}$, accounting for 61-80% during the simulation periods. Furthermore, regional transport was also an important contributor to $PM_{2.5}$ (8-35%), SOC (14-63%), and SO_4^{2-} (13-30%), with the major contribution attributed to direct transport (Fig. S5d).

3.3 Response of nitrate to IPRs

Fig. S6 illustrates the spatial distributions of $NO_3^-/PM_{2.5}$, NO_3^-/TNO_3, the nitrogen oxidation ratios (NOR= $[NO_3^-]/([NO_3^-] + [NO_2])$) and adjusted gas ratio (adjGR = $([NH_3] + [NO_3^-])/([HNO_3] + [NO_3^-])$). NOR is used to reflect the conversion efficiency of NO_2 to NO_3^-, and adjGR is used to determine the limiting factor of NO_3^- formation (Huang et al., 2021a). When the value of adjGR is greater than zero, indicating that NO_3^- is produced in HN_3-rich regime.

In Fig. S7, vertical advection and diffusion (VTRA) processes act as mainly positive contributor to NO_3^- production from 10:00 to 17:00 within model layers 1-8 (from the ground to 800m), while the IPR of the AERO process for NO_3^- is negative. Whereas, the AERO process for NO_3^- is positive at day, thus indicating that TNO_3 are partitioned into the particle phase and resulted in NO_3 accumulation upper layers 8.

In Fig. S8, the TNO_3 production rate through the OH+NO2 pathway is dominant at model layer 1 and decreases with altitude at vertically layers. In Fig. S8 (a, b), the rates and contribution of the HET N2O5 pathway is the largest in model layer 2-6 (residual layer, ~120-500 m) in winter of 2017 in Shanghai.

3.4 Production pathways of nitrate

In January, April, July and October 2017, the IRR analysis is used to elucidate the precise rates for TNO_3 formation and the relative contribution of three major TNO_3 pathways within the PBL under base, local and regional (sum of indirect and direct) transport simulations in Figs 6 and 7. Moreover, the seasonal and annual rates of the TNO_3 production pathways in five selected cities are illustrated in Table 4. Table 7 shows the comparison of the contribution of the major TNO_3 production pathways studies in the major Chinese regions. In addition, the average rates of the TNO_3 production pathways from the Local and Transport contributions in four seasons are illustrated in Tables S7 and S8.

Besides, $OH+NO_2$ pathway contribute significant to TNO_3 production in winter, accounting and 83%-88.4% at day in five YRD cities. Qin et al., (2021) has reported that the strong AOC in summer (4.5×10^{-4} min^{-1}) is 7 times higher than the average value in winter (6.4×10^{-5} min^{-1}) in YRD. Overall, local $OH+NO_2$ pathway strongly dominates the TNO_3 production rates and its diurnal variations at day, while indirect-transport HET N_2O_5 pathway has a considerable contribution at night. Consistent with the results in Section 3.2, indirect transport act as the important contributor to NO_3^- formation in the four seasons, accounting for 24-37% in the entire YRD region. The analysis of TNO_3 production pathways reveal the key precursors for TNO_3 chemical production, mainly including the locally-emitted NO_2, NH_3 and OH, as well as the locally-emitted NO_2 and transported O_3 at night. Thus, the effective control strategies to modulate NO_3^- pollution should focus on reducing locally-emitted OH and transported-O_3, besides enhancing control of NH_3 and NOx emission, especially in winter.

Tables

Table S1 WRF model configurations in this study

WRF ersion 4.2	Settings	Reference
Microphysics	New Thompson et al. scheme	Thompson et al. (2008)
Radiation Longwave Radiation	RRTM longwave scheme	Iacono et al. (2008)
Radiation Shortwave Radiation	RRTMG shortwave scheme	Iacono et al. (2008)
Surface Layer	Mellor-Yamada-Janjic similarity	
Land Surface	Noah Land Surface Model	
Planetary Boundary layer	Mellor-Yamada-Janjic scheme	Janjić (1994)
Cumulus Parameterization	Modified Tiedtke scheme	Zhang et al. (2011)
Land Surface	Noah Land Surface Model	

Table S2. Physical and chemical processes considered in CMAQ v5.2 Integrated Process Rate (IPR).

Processes ID	Name	Descriptions
1	AERO	Change due to aerosols processes, including condensation, coagulation, new particle formation and aerosol growth
2	CHEM	Net sum of all gas-phase chemical processes for species
3	CLDS	Change due to cloud processes, including aqueous reaction and removal by clouds and rain
4	Deposition	Sum of dry deposition
5	EMIS	Emissions contribution to concentration
6	HTRA	Sum of horizontal advection and diffusion
7	VTRA	Sum of vertical advection and diffusion

Notes: DDEP = Deposition; TRAN = HTRA + VTRA. The IRR of $PM_{2.5}$ major components units (μgm^{-3} h^{-1}), while the IRR of gas pollutants units (ppb h^{-1}).

Table S3. TNO_3 production reactions considered in CMAQ v5.2 Integrated Reaction Rate (IRR).

Reaction ID	Name	Descriptions
1	$OH + NO_2$	$NO_2 + OH \rightarrow HNO_3$
2	HET NO_2	$NO_2 \rightarrow 0.5*HONO + 0.5*HNO_3$
3	$N_2O_5 + H_2O$	$N_2O_5 + H_2O \rightarrow 2*HNO_3$
4	HET N_2O_5	i. N2O5 → HNO3 + H2NO3PIJ； ii. N2O5 → HNO3 + H2NO3PK； iii. H2NO3PIJ → HNO3； iv. H2NO3PK → HNO3
5	$NO_3 + HO_2$	$NO_3 + HO_2 \rightarrow 0.8*OH + 0.8*NO_2 + 0.2*HNO_3$
6	NO_3 + Org	(HCHO+CCHO+RCHO+GLY+MGLY+CRES+BALD+IPRD+HOCCHO+ACROLE+MACR+NIT1) + $NO_3 \rightarrow HNO_3$
7	HET_NO_3	$NO_3 \rightarrow HNO_3$
8	HNO3fromHydroly	i. AMTNO3J → HNO3 + 1.00*AMTHYDJ; ii. AISOPNNJ → 2.0*HNO3 + 0.5*AMTHYDJ

Notes: Three major TNO3 production pathways selected were $OH+NO_2$, HET N_2O_5, and Others. Others represent the sum of reaction 2, 3, 5, 6, 7 and 8 in this study. IRRs unit (ppb/h). Conceptual TNO_3 chemical reactions pathways can be clearly discussed in Section S1.1.

Table S4. The mean bias (MB), normalized mean bias (NMB), normalized mean error (NME), correlation coefficient (R), root mean square error (RMSE) and index of agreement (IOA) were applied to estimate the performance of the model in this study.

Statistical metrics / abbreviation	Note	Benchmarks
$MB = \frac{1}{N}\sum_{i=1}^{N}(Mi - Oi)$	Concentration unit	
$NMB = \frac{1}{N}\sum_{i=1}^{N}(\frac{Mi - Oi}{Mi + Oi})$	-1≤NMB≤+∞	NMB ≤±0.6
$NME = \frac{1}{N}\sum_{i=1}^{N}\lvert\frac{Mi - Oi}{Mi + Oi}\rvert$	0≤ NME ≤+∞	NME ≤ 0.75
$R = \frac{\sum_{i=1}^{N}(M_i - \overline{M}) \cdot (O_i - \overline{O})}{\sqrt{\sum_{i=1}^{N}(M_i - \overline{M})^2} \cdot \sqrt{\sum_{i=I}^{N}(O_i - \overline{O})^2}}$	-1 ≤ R ≤ 1	R ≥ 0.7
$RMSE = \sqrt{\sum_{i=1}^{N}\frac{(M_i - O_i)^2}{N}}$	Concentration unit	RMSE ≤ 2.0
$IOA = 1 - \frac{\sum_{i=1}^{N}(M_i - O_i)^2}{\sum_{i=1}^{N}(\lvert M_i - M_{\text{mean}}\rvert + \lvert O_i - O_{\text{mean}}\rvert)^2}$	0 < IOA ≤ 1	IOA ≥ 0.7

Note: M_i and O_i represent the concentration from modeling simulation and observation, respectively. *N* is the number of days. The benchmarks of WRF-CMAQ were suggested by Huang et al. (2021), Emery et al. (2017) and Emery et al. (2001).

Table S5. The average NO_3^- (HNO_3) concentrations for the enter YRD region under four scenarios during the modeling period. NO_3^- (HNO_3) units μg m^{-3} (ppb).

Scenarios	January	April	July	October	Annual
Base	15.95 (0.09)	7.38 (1.04)	0.95 (1.37)	5.43 (0.55)	7.43 (0.76)
YRD-zero	4.06 (0.62)	0.45 (0.65)	0.07 (0.34)	0.63 (0.36)	1.31 (0.49)
Outside-zero	8.05 (0.06)	4.58 (0.69)	0.55 (1.03)	3.15 (0.42)	4.08 (0.55)
All-zero	0.02 (0.03)	0.01 (0.05)	0.01 (0.05)	0.03 (0.01)	0.03 (0.02)

Table S6. The average rates of the important TNO_3 production pathways during the daytime and nighttime in four seasons of 2017 in Shanghai.

Production	January			April			July			October		
Rates (ppb/h)	Daily	Day	Night	Daily	Day	Night	Daily	Day	Night	Daily	Day	Night
TNO_3	0.31	0.40	0.22	0.65	0.93	0.37	1.09	1.65	0.53	0.28	0.44	0.12
OH + NO2	0.22	0.36	0.08	0.53	0.91	0.16	0.90	1.61	0.19	0.24	0.42	0.06
HET N2O5	0.09	0.04	0.14	0.10	0.01	0.19	0.12	0.01	0.26	0.03	0.01	0.05

Table S7. The average rates of the important TNO_3 production pathways during the daytime and nighttime in January, April, July and October 2017 under the Local contribution.

Production	January			April			July			October		
Rates (ppb/h)	Daily	Day	Night	Daily	Day	Night	Daily	Day	Night	Daily	Day	Night
TNO_3	0.27	0.37	0.16	0.56	0.85	0.28	1.00	1.60	0.50	0.26	0.41	0.11
OH + NO2	0.20	0.33	0.07	0.49	0.83	0.14	0.89	1.55	0.24	0.23	0.40	0.06
HET N2O5	0.07	0.03	0.09	0.07	0.02	0.11	0.11	0.02	0.20	0.03	0.01	0.04

Table S8. The average rates of the important TNO_3 production pathways during the daytime and nighttime in January, April, July and October 2017 under the Transport contribution.

Production	January			April			July			October		
Rates (ppb/h)	Daily	Day	Night	Daily	Day	Night	Daily	Day	Night	Daily	Day	Night
TNO_3	0.04	0.04	0.04	0.08	0.07	0.09	0.03	0.02	0.05	0.02	0.02	0.01
OH NO2	0.02	0.03	0.01	0.04	0.06	0.02	0.01	0.01	0.03	0.01	0.018	0.002
HET N2O5	0.02	0.01	0.03	0.04	0.01	0.06	0.02	0.003	0.04	0.01	0.002	0.01

Figures

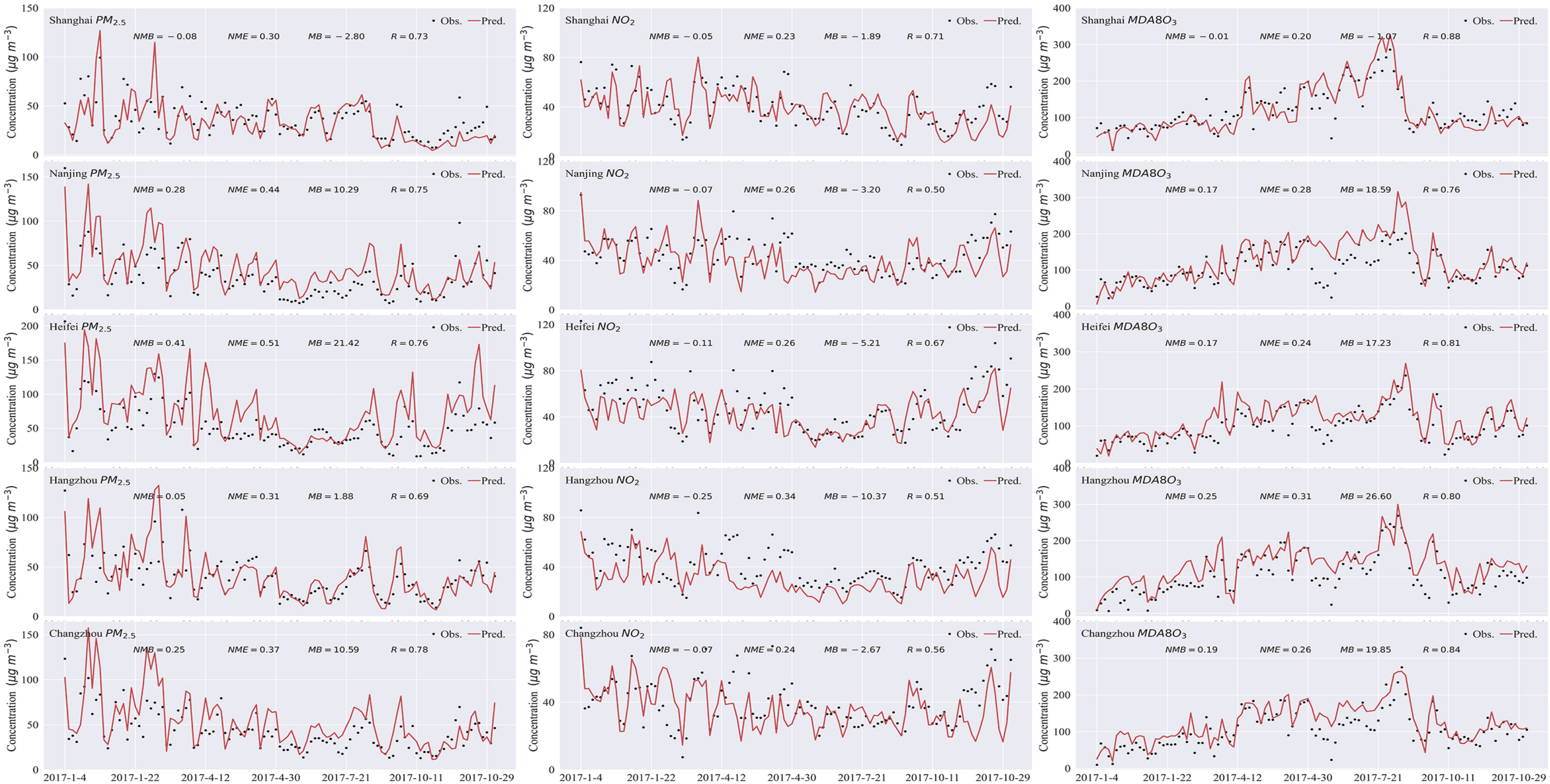

Fig. S1. Daily time series of prediction (red) and observation (black) $PM_{2.5}$, NO_2, O_3 concentrations for the full year of 2017 in five selected cities.

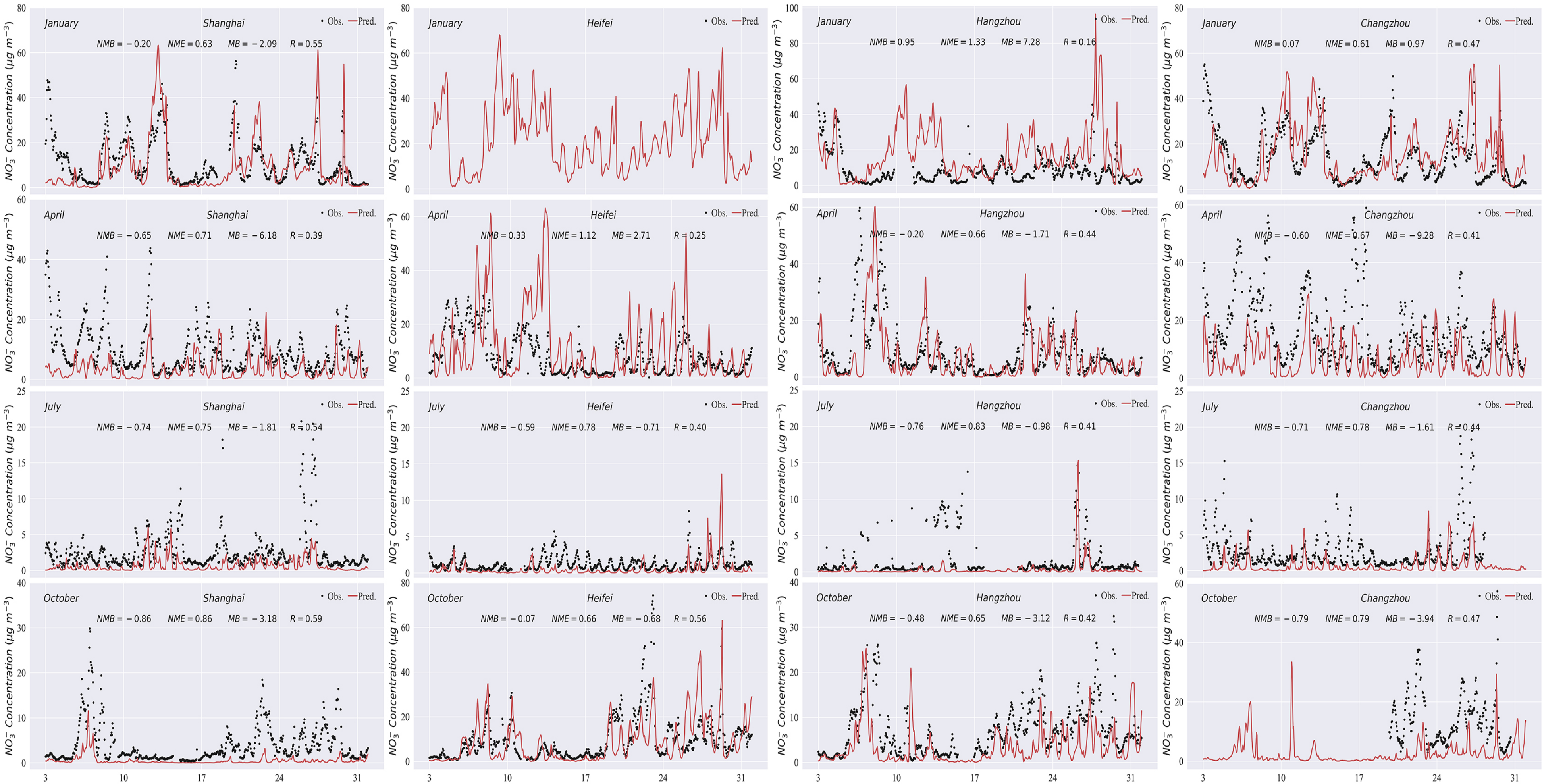

Fig. S2. Hourly time series of prediction (red) and observation (black) NO_3^- concentrations in January, April, July, and October 2017 in four cities.

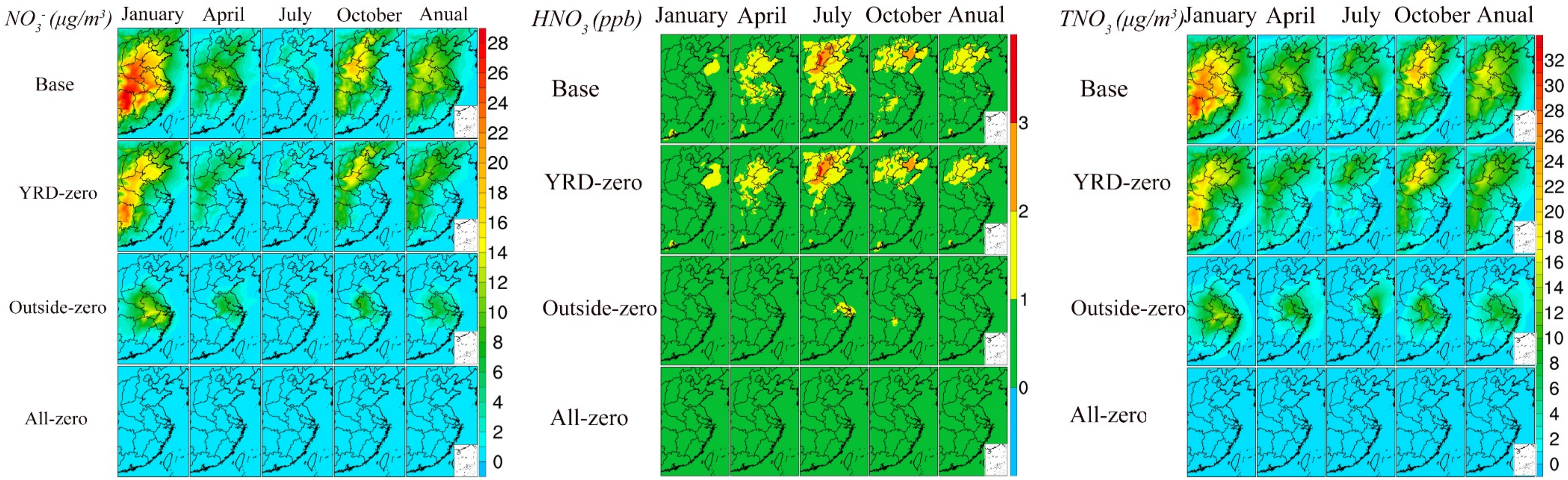

171

172 **Fig. S3.** Spatial distributions of four typical months and annual mean NO_3^-, HNO_3 and TNO_3 concentrations under four emissions scenarios.

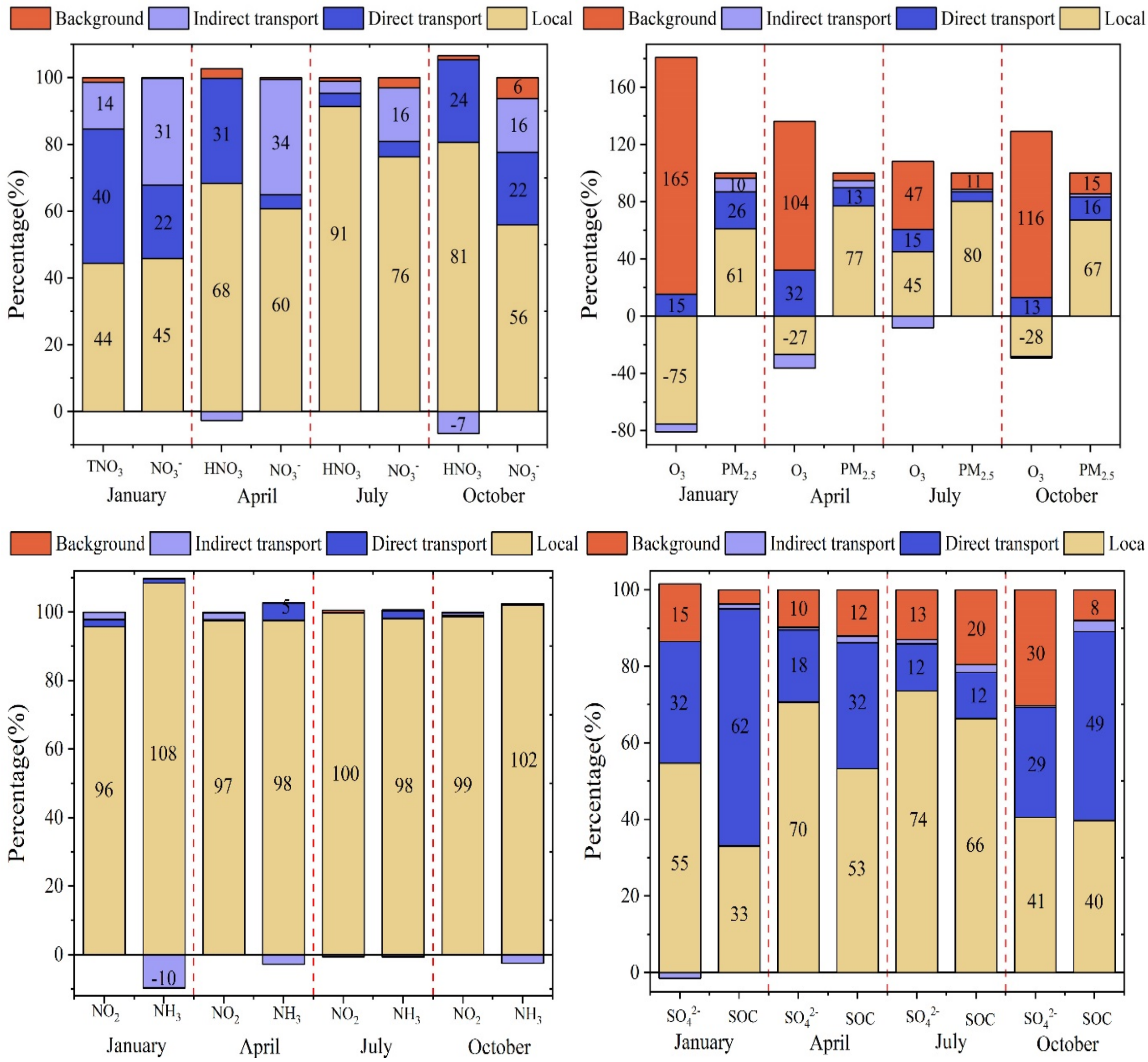

Fig. S4. The contributions of Background, Local, Indirect and Direct transport to Nitrate-related species (ie, NO_3^-, HNO_3, $PM_{2.5}$, O_3 NO_2, NH_3, SO_4^{2-} and SOC) in January, April, July and October 2017 in Shanghai.

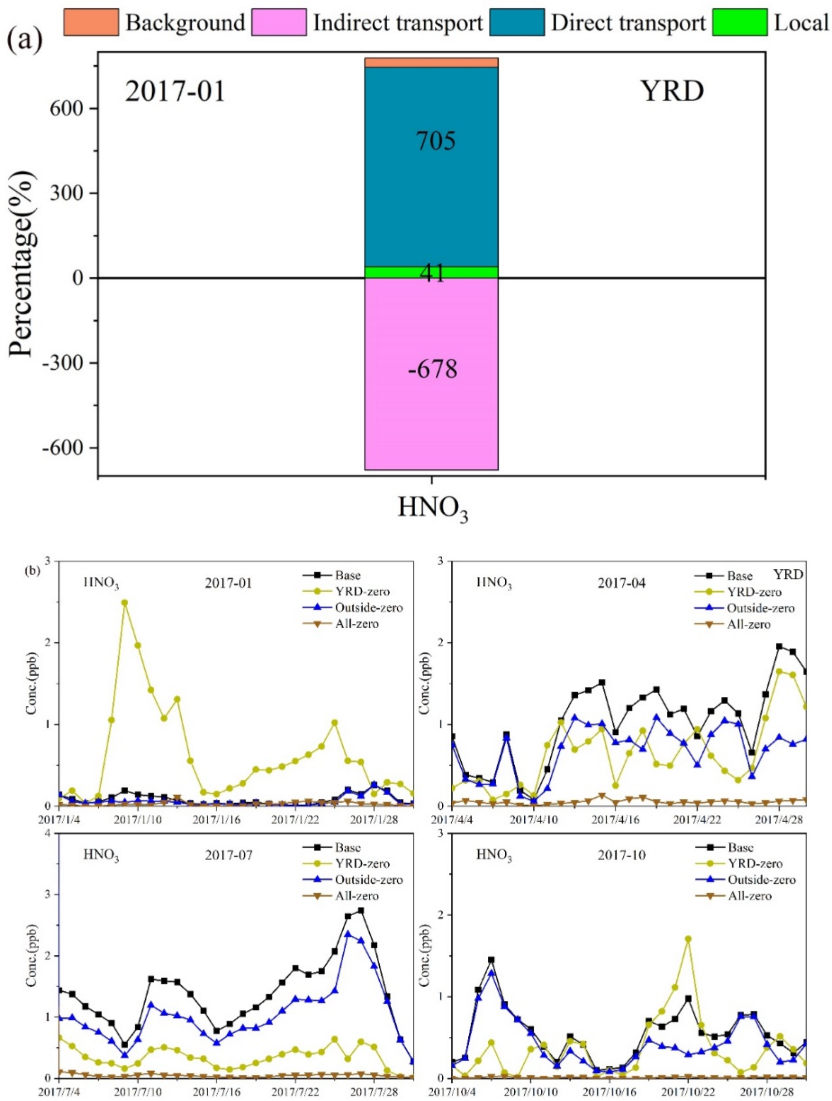

Fig. S5. (a). The contributions of Background, Local, Indirect and Direct transport to HNO_3 in January 2017 for the enter YRD; (b). The concentrations of HNO_3 concentrations during the simulation period under four scenarios for the enter YRD.

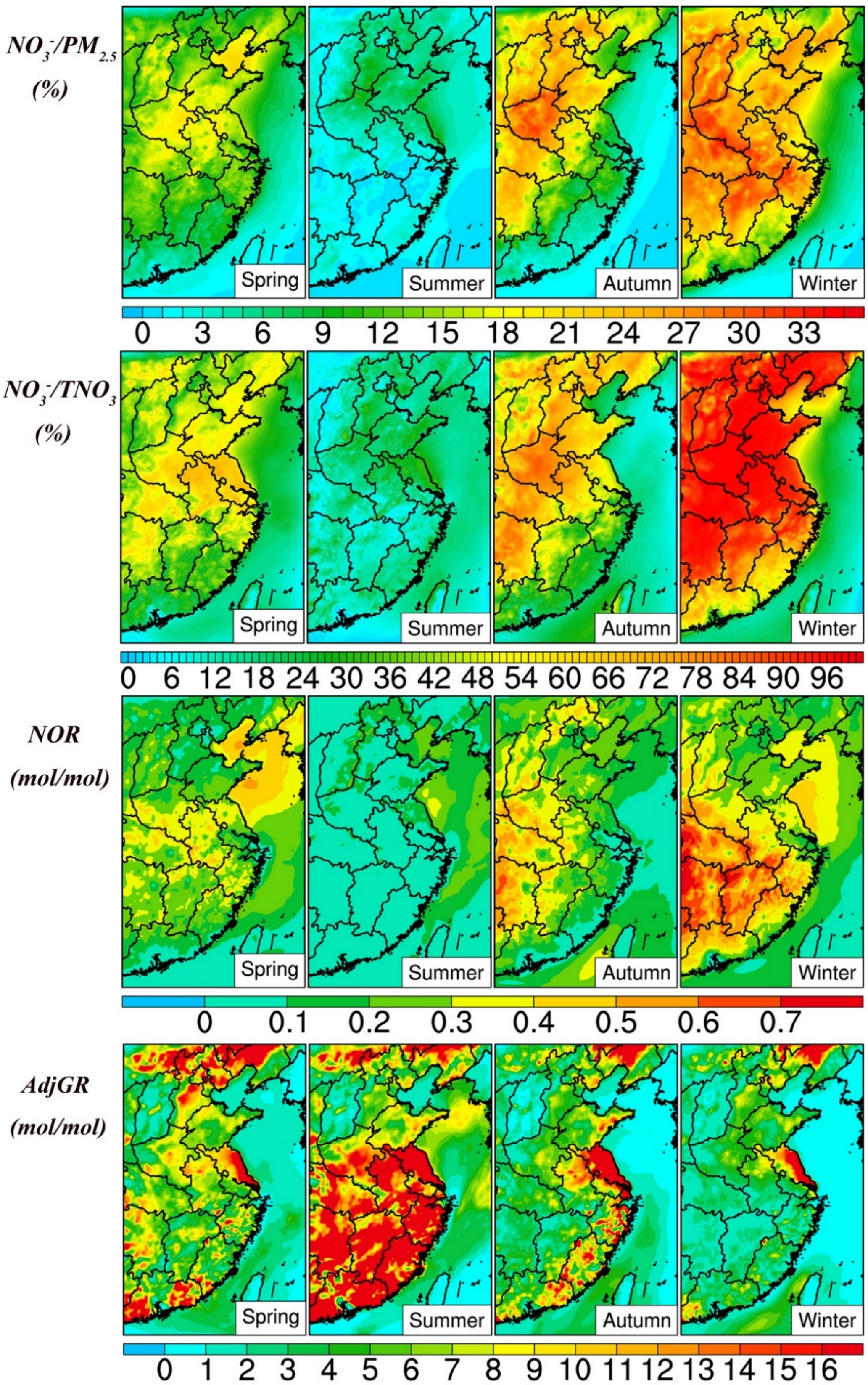

Fig. S6. Spatial distributions of four typical seasons of $NO_3^-/PM_{2.5}$, NO_3^-/TNO_3, NOR and AdjGR under base scenario.

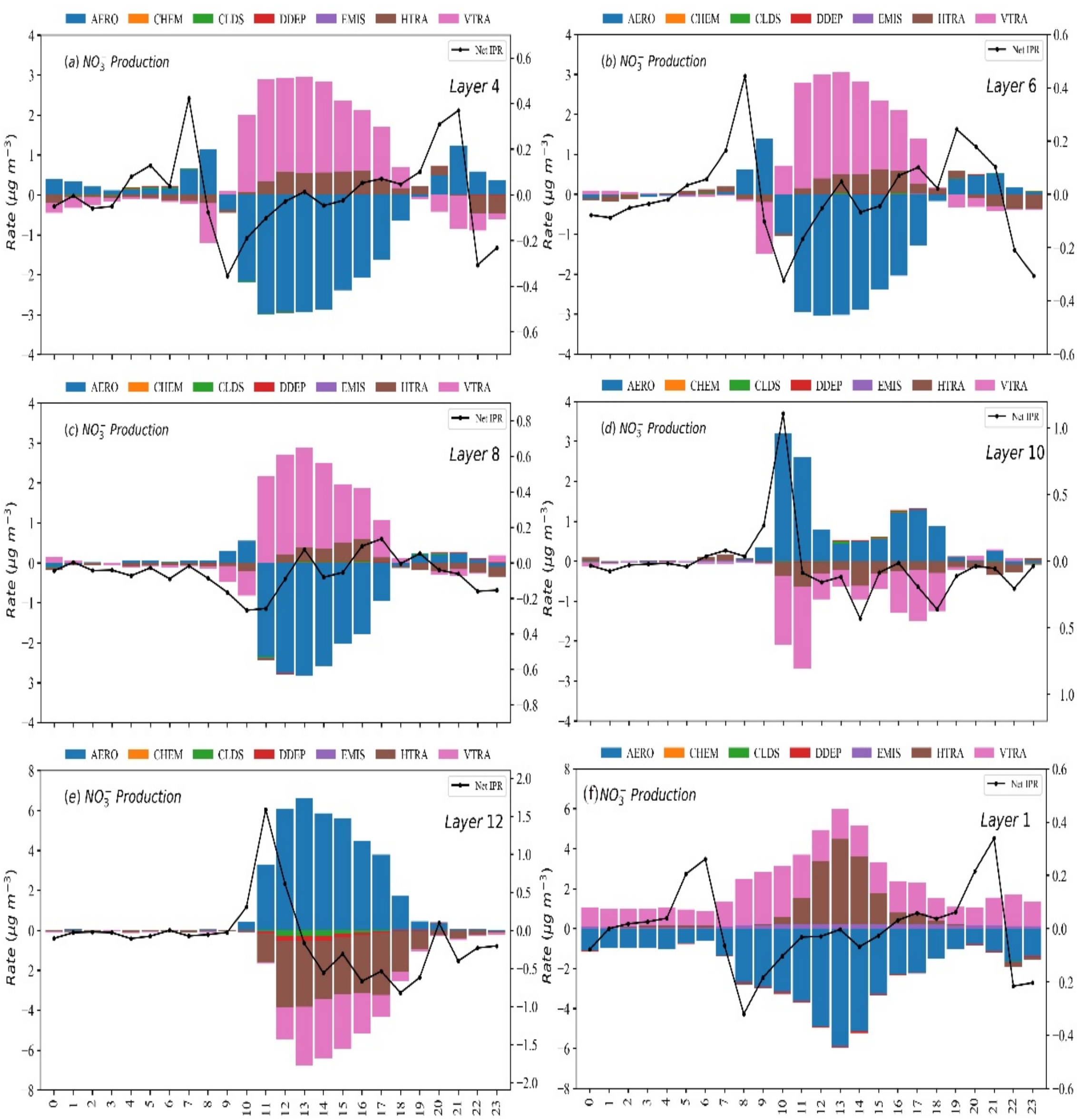

Fig. S7. Vertical layers (Layer 1, 4, 6, 8, 10 and 12) physical and chemical processes rates NO_3^- in July 2017. The black line represents the net IPR value in each hour of day.

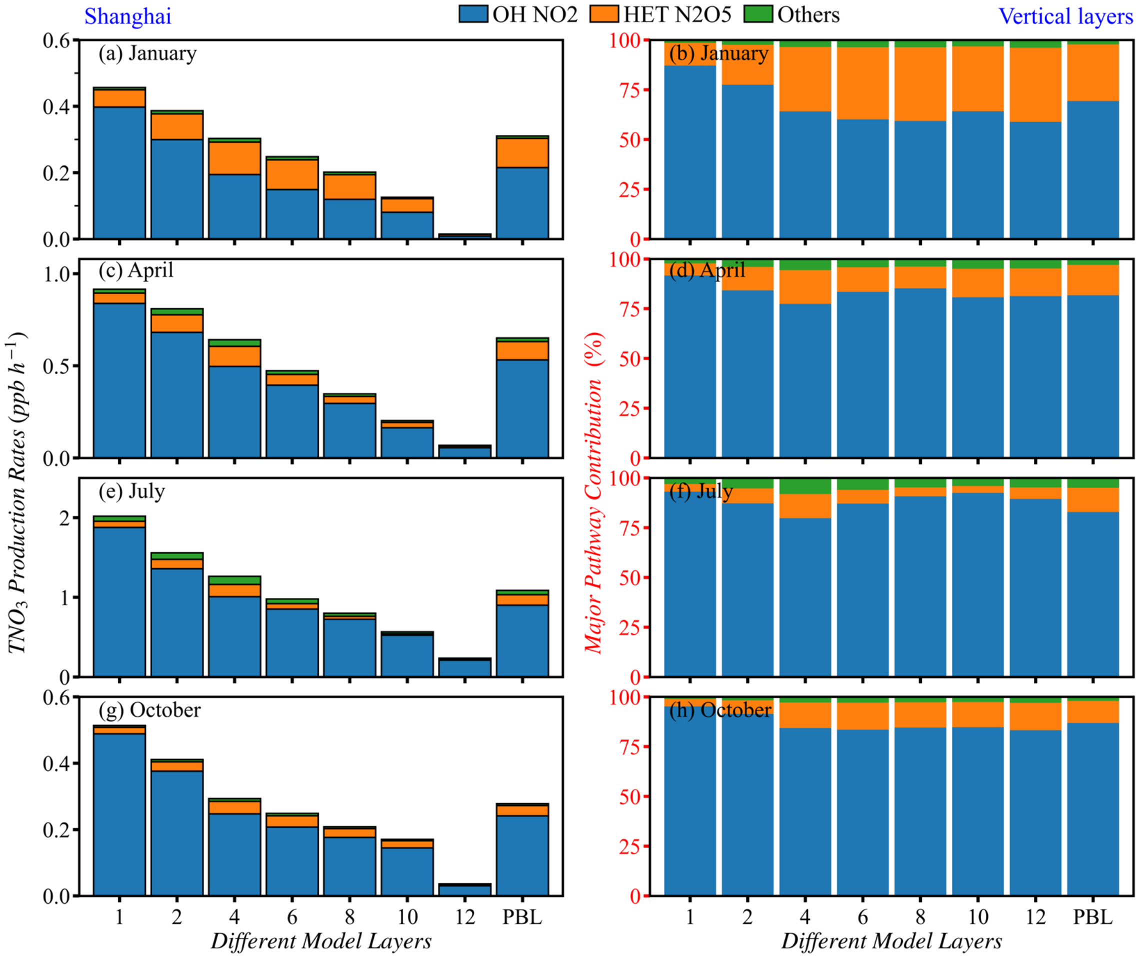

Fig. S8. Comparison of TNO_3 production rates (a, c, e, g) and contributions (b, d, f, h) of three major pathways between vertical layers (Layer 1, 4, 6, 8, 10 and 12, corresponding to the height ranging from 32 to 80 m, 80 to 160 m, 250 to 320 m, 420 to 500 m, 580 to 760 m, 1000 to 1300 m, and 2000 to 2800 m, respectively) and PBL.

References

Hu, J., Chen, J., Ying, Q., Zhang, H., 2016. One-year simulation of ozone and particulate matter in China using WRF/CMAQ modeling system. Atmos. Chem. Phys. 16, 10333-10350.

Liu, T., Wang, X.Y., Hu, J.L., Wang, Q., An, J., Gong, K., Sun, J., Li, L., Qin, M., Li, J., Tian, J., Huang, Y., Liao, H., Zhou, M., Hu, Q., Yan, R., Wang, H., Huang, C., 2020. Driving Forces of Changes in Air Quality during the COVID-19 Lockdown Period in the Yangtze River Delta Region, China. Environ. Sci. Technol. Lett. 7, 779-786.

Wang, X., Li, L., Gong, K., Mao, J., Hu, J., Li, J., Liu, Z., Liao, H., Qiu, W., Yu, Y., Dong, H., Guo, S., Hu, M., Zeng, L., Zhang, Y., 2021. Modelling air quality during the EXPLORE-YRD campaign – Part I. Model performance evaluation and impacts of meteorological inputs and grid resolutions. Atmos. Environ. 246, 118131.

Huang, L., Zhu, Y., Zhai, H., Xue, S., Zhu, T., Shao, Y., Liu, Z., Emery, C., Yarwood, G., Wang, Y., Fu, J., Zhang, K., Li, L., 2021. Recommendations on benchmarks for numerical air quality model applications in China – Part 1: PM2.5 and chemical species. Atmos. Chem. Phys. 21, 2725-2743

Emery, C., Liu, Z., Russell, A.G., Odman, M.T., Yarwood, G., Kumar, N., 2017. Recommendations on statistics and benchmarks to assess photochemical model performance. J. Air Waste Manage. Assoc. 67, 582-598.

Emery, C., Tai, E., Yarwood, G., 2001. Enhanced Meteorological Modeling and Performance Evaluation for Two Texas Ozone Episodes, Prepared for the Texas Natural Resource Conservation Commission. Environ International Corporation, Novato, CA.

Qin, M., Hu, A., Mao, J., Li, X., Sheng, L., Sun, J., Li, J., Wang, X., Zhang, Y., and Hu, J.: PM2.5 and O3 relationships affected by the atmospheric oxidizing capacity in the Yangtze River Delta, China, Sci. Total Environ., 152268, https://doi.org/10.1016/j.scitotenv.2021.152268, 2021.

Huang, L., Sun, J. J., Jin, L., Brown, N. J., and Hu, J.: Strategies to reduce PM2.5 and O3 together during late summer and early fall in San Joaquin Valley, California, Atmos. Res., 258, 105633, https://doi.org/10.1016/j.atmosres.2021.105633, 2021a.

Iacono, M.J., Delamere, J.S., Mlawer, E.J., Shephard, M.W., Clough, S.A., Collins, W.D., 2008. Radiative forcing by long-lived greenhouse gases: Calculations with the AER radiative transfer models. Journal of Geophysical Research: Atmospheres 113.

Janjić, Z.I., 1994. The Step-Mountain Eta Coordinate Model: Further Developments of the Convection, Viscous Sublayer, and Turbulence Closure Schemes. MWRv 122, 927-945.

Thompson, G., Field, P.R., Rasmussen, R.M., Hall, W.D., 2008. Explicit Forecasts of Winter Precipitation Using an Improved Bulk Microphysics Scheme. Part II: Implementation of a New Snow Parameterization. MWRv 136, 5095-5115.

Zhang, C., Wang, Y., Hamilton, K., 2011. Improved Representation of Boundary Layer Clouds over the Southeast Pacific in ARW-WRF Using a Modified Tiedtke Cumulus Parameterization Scheme. MWRv 139, 3489-3513.